ELSEVIER

International Journal of Heat and Fluid Flow 20 (1999) 563–573

International Journal of HEAT AND FLUID FLOW

www.elsevier.com/locate/ijhff

Modeling rotational effects in eddy-viscosity closures

B.A. Pettersson Reif [a,*], P.A. Durbin [b], A. Ooi [a]

[a] *Center for Turbulence Research, Stanford University, Stanford, CA 94305-3030, USA*
[b] *Mechanical Engineering Department, Stanford University, Stanford, CA 94305-3030, USA*

Received 8 April 1999; accepted 26 July 1999

Abstract

A new approach to sensitize turbulence closures based on the linear eddy-viscosity hypothesis to rotational effects is proposed. The principal idea is to 'mimic' the behavior of a second moment closure (SMC) in rotating homogeneous shear flow; depending on the ratio of the mean flow to the imposed rotational time scales, the model should be able to bifurcate between two stable equilibrium solutions. These solutions correspond to exponential or algebraic time dependent growth or decay of turbulent kinetic energy. This fundamental behavior of SMCs is believed to be of importance also in the prediction of non-equilibrium turbulence. A near-wall turbulence model which is based on the linear eddy-viscosity hypothesis is modified in the present study. Wall proximity effects are modeled by the elliptic relaxation approach. This closure has been successfully applied in the computation of complex, non-equilibrium flows in inertial frames of reference. The objective of the present study is to extend the predictive capability of the model to include flows dominated by rotational effects. The new model is calibrated in rotating homogeneous turbulent shear flow and subsequently tested in three different cases characterized by profound effects of system rotation or streamline curvature. It is able to capture many of the effects due to imposed body forces that the original closure is incapable of. Good agreement is obtained between the present predictions and available experimental and DNS data.

Keywords: Eddy-viscosity; Bifurcation diagram; System rotation; Streamline curvature; Homogeneous turbulence; Near-wall turbulence; Elliptic relaxation

Notation

C_f	skin friction coefficient, $\tau_w/\frac{1}{2}\rho U_b^2$
C_μ, C_μ^*	eddy-viscosity coefficients
f	intermediate variable, Eq. (3)
h	channel or step height
k	turbulent kinetic energy, $\frac{1}{2}\overline{u_i u_i}$
L	turbulent length scale, Eq. (5)
P	mean pressure or mean shear generation rate of k, Eq. (4)
P^*	mean reduced pressure, $P - \frac{1}{2}\Omega^2 x_i x_i$
$\mathscr{R}$	non-dimensional parameter, $\sqrt{\eta_2/\eta_1}$
R_c	radius of curvature
Re	Reynolds number, $2hU_b/\nu$
Re_m	Reynolds number, $\delta_2 U_\infty/\nu$
Re_*	Reynolds number, hu_*/ν
Ro	rotation number, $2h\Omega/U_b$
S	mean shear rate, $(S_{ij}S_{ij})^{1/2}$
S_{ij}	mean rate of strain tensor, $\frac{1}{2}(\partial_j U_i + \partial_i U_j)$
S_{ij}^*	non-dimensional strain rate tensor, Eq. (10)
T	turbulent time scale, Eq. (5)
U_b	mean bulk velocity
U_i	mean velocity in the x_i-direction, $[U, V, W]$
U_{pw}	potential flow mean velocity, $\lim_{y\to\infty}(\alpha U)$
u_*	wall friction velocity, $(\tau_w/\rho)^{1/2}$
$\overline{u_i u_j}$	kinematic Reynolds stress tensor
v^2	turbulent velocity scale, Eq. (3)
W_{ij}	mean intrinsic vorticity tensor, $\frac{1}{2}(\partial_j U_i - \partial_i U_j) + \epsilon_{jik}\Omega_k$
W_{ij}^*	non-dimensional vorticity tensor, Eq. (10)
x_i	Cartesian coordinate, $[x, y, z]$

Greek

α	curvature parameter, $1 + y/R_c$
δ_2	momentum thickness
δ_{ij}	Kronecker delta
ε	dissipation rate of k
ϵ_{ijk}	cyclic permutation tensor
η_i	non-dimensional velocity gradient invariant, Eqs. (9) and (19)
Ω_k	angular frame velocity about the x_k-axis
ν	kinematic viscosity
ν_t	eddy viscosity, Eq. (4)

1. Introduction

The majority of turbulent flows of engineering interest are characterized by non-equilibrium turbulence as well as by

* Corresponding author. Present address: Kongsberg Defence and Aerospace, N-3601, Kongsberg, Norway.
E-mail address: bjornr@ctr.stanford.edu (B.A. Pettersson Reif)

0142-727X/99/$ - see front matter
PII: S0142-727X(99)00056-9

effects of inertial forces, such as arise from imposed rotation of the reference frame, or from streamline curvature. This imposes high demands on turbulence models employed in CFD codes: reliable, yet cost effective, flow predictions are required under complex conditions. It is therefore unfortunate that the most commonly used closure scheme, the k–ε model, suffers from an inability to account for crucial non-equilibrium effects.

Numerous experimental and numerical investigations have established that body forces arising from imposed system rotation or from streamline curvature can substantially alter both the mean flow field and the intensity and structure of the turbulence. The most natural level of closure modeling to adopt in these cases is Second-Moment Closure (SMC), which in a natural and systematic manner accounts for rotation. The potential advantage of SMC stems from the appearance of exact production terms due to mean flow gradients and system rotation. The full SMC equations also contain convective and dispersive transport of the second moments. This modeling approach is physically more appealing than the eddy-viscosity concept, but it is still not tractable in complex industrial applications, due to excessive computational cost and computational stiffness.

Renewed attention has recently been paid to algebraic stress modeling. This is an alternative to the full SMC, formally justified in turbulent flows not too far from equilibrium. In fact, explicit algebraic stress models (EASM) can systematically be derived by solving SMCs in the limit of equilibrium homogeneous turbulence (Pope, 1975). In these solutions the dependence of the Reynolds stresses on system rotation is retained. Although the EASMs are based on arguments formally valid only in equilibrium flows, Speziale and Abid (1995) demonstrated that such models could provide reasonable predictions in some non-equilibrium flows.

The most frequently adopted turbulence closures in industrial computations invoke the linear eddy-viscosity hypothesis for the mean flow and scalar transport equations for the turbulence – e.g., the k–ε model. An inherent shortcoming of these models is their property of material frame indifference; in other words, they are independent of imposed system rotation. A common practice in sensitizing such models to non-inertial effects is to modify the turbulent length scale by adding rotation dependent terms to the dissipation rate equation (Howard et al., 1980). Although the dissipation rate model equation is based more on intuition than on rigorous arguments, it still exhibits a surprising degree of generality. Therefore, there exists a reluctance to introduce ad hoc rotation terms into the ε transport equation.

The present paper describes a rather different method. A modified eddy viscosity formula is developed, guided by an EASM solution. This formula is constrained to reduce to the original, scalar model in non-rotating flow. EASM solutions do not satisfy this constraint. Without it, significant alterations to the original model will occur even in non-rotating flows; these can deteriorate the predictions of a well-calibrated model.

The methodology described herein can be applied to any scalar eddy viscosity model. We will work with the v^2–f model instead of a k–ε variant. A well known failing of k–ε is that the turbulent kinetic energy k is not the appropriate velocity scale close to solid boundaries. The k–ε eddy viscosity significantly overpredicts turbulent transport in the proximity of a wall. The remedy usually taken is to introduce ad hoc damping functions. These functions frequently cause numerical stiffness, and give poor predictions in complex flows.

Durbin (1991) proposed to replace the turbulent kinetic energy k by a better behaved velocity scale ($\overline{v^2}$) and subsequently introduced the $\overline{v^2}$–f model. This model can be thought of as a subset of a full Second-Moment Closure (SMC) in the sense that $\overline{v^2}$ is analogous to the wall-normal Reynolds stress near to surfaces. However, $\overline{v^2}$ is not the component of a tensor; it is a scalar that represents an appropriate turbulent velocity scale in the near-wall region. Kinematic blocking of turbulent transport close to a solid boundary is provided indirectly by solving an elliptic relaxation equation for f, which is a source in the $\overline{v^2}$-equation. The governing set of equations in the $\overline{v^2}$–f model is integrated all the way to the wall.

The $\overline{v^2}$–f model has performed well in a wide number of turbulent flows, ranging from flat plate boundary layers to massive separation (Parneix et al., 1998). However, it is a scalar model, so it too exhibits material frame indifference.

2. Turbulence modeling

Following Pope (1975), the most general tensor function of the mean deformation rate tensors can be written in two dimensions as

$$\frac{\overline{u_i u_j}}{k} = \frac{2}{3}\delta_{ij} - aS_{ij} - b(S_{ik}W_{kj} - W_{ik}S_{kj}) - c(S_{ij}^2 - \tfrac{1}{3}|S^2|\delta_{ij}) \tag{1}$$

for a constant property, incompressible fluid. In general the coefficients a, b and c are functions of the invariants $|S^2| \equiv S_{ik}S_{ki}$ and $|W^2| \equiv W_{ik}W_{ki}$, as well as of scalar properties of the turbulence field. The most frequently used constitutive relation retains only terms up to first order ($b = c = 0$), where the free coefficient is often stated as $a = 2C_\mu k/\varepsilon$. This formulation is computationally very attractive since it promotes numerical stability (provided that the eddy-viscosity remains positive). The $\overline{v^2}$–f model uses

$$\frac{\overline{u_i u_j}}{k} = \frac{2}{3}\delta_{ij} - 2C_\mu^* \frac{\overline{v^2}}{k} T\, S_{ij}, \tag{2}$$

where T is a turbulent time scale and the scalar $\overline{v^2}$ is obtained from a transport equation. The introduction of $\overline{v^2}/k$ in (2) provides a measure of turbulence anisotropy, which plays a crucial role in near-wall flows.

The modeled set of transport equations for the $\overline{v^2}$–f model are

$$\begin{aligned}
\frac{\mathrm{D}k}{\mathrm{D}t} &= P - \varepsilon + \frac{\partial}{\partial x_j}\left((\nu + \nu_t)\frac{\partial k}{\partial x_j}\right),\\
\frac{\mathrm{D}\varepsilon}{\mathrm{D}t} &= \frac{C_{\varepsilon 1}^* P - C_{\varepsilon 2}\varepsilon}{T} + \frac{\partial}{\partial x_j}\left(\left(\nu + \frac{\nu_t}{\sigma_\varepsilon}\right)\frac{\partial \varepsilon}{\partial x_j}\right),\\
\frac{\mathrm{D}\overline{v^2}}{\mathrm{D}t} &= kf - \frac{\overline{v^2}}{k}\varepsilon + \frac{\partial}{\partial x_j}\left((\nu + \nu_t)\frac{\partial \overline{v^2}}{\partial x_j}\right),\\
f - L^2\nabla^2 f &= (C_1 - 1)\frac{2/3 - \overline{v^2}/k}{T} + C_2\frac{P}{k},
\end{aligned} \tag{3}$$

where

$$\nu_t = C_\mu^* \overline{v^2} T, \quad P = 2\nu_t|S^2| \tag{4}$$

and

$$\begin{aligned}
L &= C_L \max\left(\frac{k^{3/2}}{\varepsilon}; C_\eta\left(\frac{\nu^3}{\varepsilon}\right)^{1/4}\right),\\
T &= \max\left(\frac{k}{\varepsilon}; 6\left(\frac{\nu}{\varepsilon}\right)^{1/2}\right).
\end{aligned} \tag{5}$$

The model coefficients are given by

$$C^*_{\varepsilon 1} = 1.4\left(1 + 0.045\sqrt{\frac{k}{\overline{v^2}}}\right), \quad C_{\varepsilon 2} = 1.9,$$
$$\sigma_\varepsilon = 1.3, \quad C_L = 0.25, \quad C_\eta = 85.0, \quad C_1 = 1.4, \quad C_2 = 0.3 \tag{6}$$

and the solid wall boundary conditions used in numerical computations are

$$U_i = 0, \quad \overline{v^2} = 0, \quad k = \partial k/\partial x_n = 0,$$
$$f_{\text{wall}} = \lim_{d\to 0}\left[\frac{-20\nu^2\overline{v^2}}{\varepsilon d^4}\right]. \tag{7}$$

The last limit is finite because $\overline{v^2} = \mathrm{O}(d^4)$ as the wall distance $d \to 0$.

2.1. Modeling rotational effects

An inherent shortcoming of the widely used linear stress–strain relationship (2), which limits its usefulness in many situations, is its inability to account for non-inertial effects on the turbulent stresses. It should be recalled that the set of transport equations governing turbulent scalars, such as k, ε and $\overline{v^2}$, do not directly depend on an imposed rotation of the reference frame; the effect of system rotation enters only indirectly through changes in the turbulence anisotropy and the mean flow field. It can, furthermore, readily be seen from (1), that rotational strains only appear explicitly in the non-linear term $S_{ik}W_{kj} - W_{ik}S_{kj}$. The apparent conclusion would seem to be that a non-linear constitutive relationship is needed in order to be able to predict non-inertial effects within the framework of eddy-viscosity modeling.

However, let us consider, for instance, unidirectional channel flow in orthogonal mode rotation, i.e. $\vec{U} = (U(y), 0, 0)$ and $\vec{\Omega} = (0, 0, \Omega)$. This is a simple benchmark to assess the performance of turbulence closures in flows affected by rotation (Launder and Tselepidakis, 1994, 1997). In this particular case rotation affects the mean flow field only indirectly through the turbulent shear stress $\overline{u_1u_2}$. Only the second term, aS_{ij}, of (1) contributes to $\overline{u_1u_2}$. Hence, in this particular case, the effect of rotation on the mean flow field enters the constitutive relation (1) solely through the linear term. Since the mean rate-of-strain tensor S_{ij} is frame-indifferent, it can be concluded that *non-inertial effects must be accommodated in the linear eddy-viscosity coefficient*.

Gatski and Speziale (1993) systematically derived an explicit solution to the Algebraic Stress representation of a linear Second-Moment Closure in a non-inertial frame of reference by the integrity basis technique. The two-dimensional solution is also a homogeneous, equilibrium solution to the original SMC. Durbin and Shabany (1997) applied this technique to the quasi-linear SSG model, in which the invariant $\overline{u_iu_j}\ \overline{u_ju_i}$ enters a coefficient. These solutions are necessarily of the form (1). The coefficient of the linear term in the explicit solution has the form

$$C^*_\mu \sim (1 - \alpha_1\eta_1 + \alpha_2\eta_2)^{-1}, \tag{8}$$

where the dimensionless velocity gradient invariants are

$$\eta_1 \equiv S^*_{ik}S^*_{ik}, \quad \eta_2 \equiv W^*_{ik}W^*_{ik} = -W^*_{ik}W^*_{ki}. \tag{9}$$

Rotational effects thus enter the constitutive relation via η_2. The non-dimensional strain-rate and vorticity tensors are defined as

$$S^*_{ik} = \frac{1}{2}T\left(\frac{\partial U_i}{\partial x_k} + \frac{\partial U_k}{\partial x_i}\right),$$
$$W^*_{ik} = \frac{1}{2}T\left[\left(\frac{\partial U_i}{\partial x_k} - \frac{\partial U_k}{\partial x_i}\right) + 2\overline{C}_\omega\epsilon_{kim}\Omega_{\text{m}}\right]. \tag{10}$$

$\overline{C}_\omega$ depends on the constants of the closure model. The present study adopts $\overline{C}_\omega = 2.25$ which is the value obtained by Gatski and Speziale (1993) for the SSG pressure–strain model. The present study also replaces the turbulent timescale k/ε, used by Gatski and Speziale (1993), by T, defined in (5).

The objective to sensitize the scalar models to effects of system rotation and streamline curvature seems possible to achieve by following (8) and expressing the eddy-viscosity coefficient as a function of the non-dimensional velocity gradient invariants, $C^*_\mu = C^*_\mu(\eta_1, \eta_2)$. Jongen et al. (1998) also concluded that it was necessary to modify C_μ. The present procedure is to use the Gatski and Speziale (1993) solution for rotating flow to guide the development of this function. Homogeneous shear flow will be used as a guide in the model development, not only to calibrate model constants, but also to ensure a physically realistic model.

2.1.1. Homogeneous flow

Although homogeneous turbulence is superficially simple, it is believed to be a useful point of reference, even for models primarily developed for complex flows far from equilibrium. Consider two-dimensional, homogeneous turbulent flow subjected to orthogonal mode rotation. In principal axes of the rate of strain

$$[\partial_j U_i] = \begin{bmatrix} S & \omega \\ -\omega & -S \end{bmatrix}$$

and the angular frame velocity is Ω. The evolution equations for the timescale ratio ε/Sk and the scalar $\overline{v^2}/k$ can then be written as

$$\frac{\mathrm{d}}{\mathrm{d}\sigma}\left(\frac{\varepsilon}{Sk}\right) = \left[\frac{P}{\varepsilon} - \frac{(C_{\varepsilon 2} - 1)}{(C^*_{\varepsilon 1} - 1)}\right]\left(\frac{\varepsilon}{Sk}\right)^2(C^*_{\varepsilon 1} - 1),$$
$$\frac{\mathrm{d}}{\mathrm{d}\sigma}\left(\frac{\overline{v^2}}{k}\right) = \frac{\varepsilon}{Sk}\left[(C_1 - 1)\left(\frac{2}{3} - \frac{\overline{v^2}}{k}\right) + \left(C_2 - \frac{\overline{v^2}}{k}\right)\frac{P}{\varepsilon}\right], \tag{11}$$

where $\sigma = St$. In the present case $P/\varepsilon = C^*_\mu\overline{v^2}/k(Sk/\varepsilon)^2$. The non-dimensional velocity gradient invariants, given by (9), can be expressed as

$$\eta_1 = 2(Sk/\varepsilon)^2, \quad \eta_2 = 2(Sk/\varepsilon)^2(\overline{C}_\omega\Omega/S - \omega/S)^2. \tag{12}$$

Insight into essential parameters characterizing the turbulence is provided by a bifurcation diagram in $\varepsilon/Sk - \eta_2/\eta_1$ phase-space (Speziale and Mac Giolla Mhuiris, 1989). Eq. (11) has two equilibria: $(P/\varepsilon)_\infty = (C_{\varepsilon 2} - 1)/(C^*_{\varepsilon 1} - 1)$ and $(\varepsilon/Sk)_\infty = 0$. At small η_2/η_1 the former is stable and the latter unstable. At a certain η_2/η_1, a bifurcation occurs, at which the former solution disappears, and the latter becomes stable. The points in the $\varepsilon/Sk - \eta_2/\eta_1$ space where these two solutions coexist are referred to as bifurcation points. The equilibrium $(\varepsilon/Sk)_\infty \neq 0$ is characterized by exponential growth of k, whereas $(\varepsilon/Sk)_\infty = 0$ is associated with a power law solution for k:

$$\text{(i) } k \sim \mathrm{e}^{\lambda t}; \quad \lambda = \frac{C_{\varepsilon 2} - C^*_{\varepsilon 1}}{C^*_{\varepsilon 1} - 1}\left(\frac{\varepsilon}{Sk}\right); \ \frac{Sk}{\varepsilon}\text{depends on model,}$$
$$\text{(ii) } k \sim t^\lambda; \quad \lambda = \frac{(P/\varepsilon) - 1}{C_{\varepsilon 2} - 1 - (P/\varepsilon)(C^*_{\varepsilon 1} - 1)};$$
$$\frac{P}{\varepsilon}\text{depends on model.} \tag{13}$$

The bifurcation is from exponential growth to algebraic growth. This is somewhat unusual: commonly a bifurcation is

associated with loss of exponential stability. However, the exponent in the power law solution is positive at the bifurcation because P/ε is greater than 1. When P/ε becomes less than 1 the turbulence decays.

The terms in (13) that are stated to depend on the model are found by evaluating

$$P/\varepsilon = -\frac{\overline{u_i u_j} S_{ij}}{\varepsilon} = \frac{\varepsilon}{k} a(\eta_1, \eta_2)\eta_1 = 2C_\mu^* \eta_1 \frac{\overline{v^2}}{k} \tag{14}$$

having used (1) for $\overline{u_i u_j}$ and (2) for the v^2–f model.

Equating P/ε to $(C_{\varepsilon 2}-1)/(C_{\varepsilon 1}^*-1)$ defines the non-trivial branch (i) of the bifurcation diagram. Eq. (14) then becomes

$$\frac{1}{\eta_1} = 2C_\mu^* \frac{\overline{v^2}}{k}\left(\frac{C_{\varepsilon 1}^*-1}{C_{\varepsilon 2}-1}\right). \tag{15}$$

The steady state of (11) provides the equilibrium formula

$$\frac{\overline{v^2}}{k} = \frac{\frac{2}{3}(C_1-1)(C_{\varepsilon 1}^*-1) + C_2(C_{\varepsilon 2}-1)}{(C_1-1)(C_{\varepsilon 1}^*-1) + C_{\varepsilon 2}-1} \tag{16}$$

that implicitly determines $\overline{v^2}/k$ (with subscripts ∞ understood). From (16) and (6) the equilibrium values $P/\varepsilon = (C_{\varepsilon 2}-1)/(C_{\varepsilon 1}^*-1) = 1.78$ and $\overline{v^2}/k = 0.367$ are obtained. Then (15) becomes

$$C_\mu^* \eta_1 = 2.425. \tag{17}$$

Inserting a given function $C_\mu^*(\eta_1, \eta_2)$ defines the curve $\eta_1 = Fcn(\eta_2/\eta_1)$ for branch (i) (see Fig. 1).

The variation of P/ε as a function of Ω/S for the power law branch (ii) is also obtained from the relation (14). On this branch $\eta_1 \to \infty$, with η_2/η_1 finite. Since P/ε is unknown, the steady state of (11) is now written

$$\frac{\overline{v^2}}{k} = \frac{\frac{2}{3}(C_1-1) + C_2 P/\varepsilon}{C_1 - 1 + P/\varepsilon}$$

and (14) becomes

$$\frac{1}{2}\left(\frac{P}{\varepsilon}\right)\frac{(C_1-1)+P/\varepsilon}{\frac{2}{3}(C_1-1)+C_2 P/\varepsilon} = \lim_{\eta_1 \to \infty} \eta_1 C_\mu^*. \tag{18}$$

The right-hand side is a function of η_2/η_1 (see Eq. (21)) giving $P/\varepsilon = Fcn(\eta_2/\eta_1)$ for branch (ii) (see Fig. 1).

It is readily seen from Eq. (15) that the original $\overline{v^2}$–f model, like any other eddy-viscosity model that retains a constant coefficient $C_\mu^* = C_\mu$, has only one equilibrium: $\varepsilon/Sk = \text{constant}$.

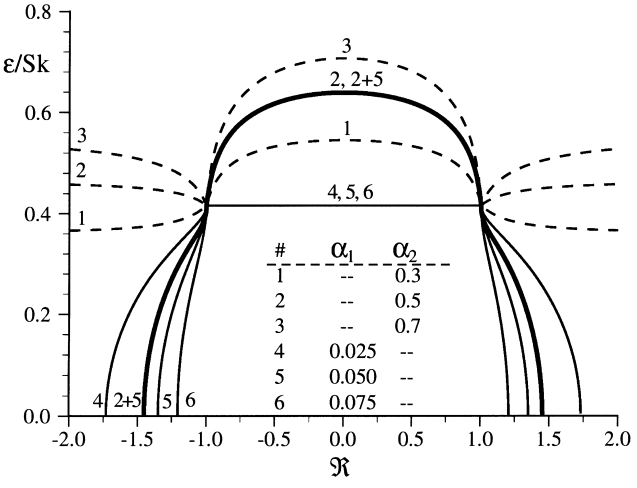

Fig. 1. Rotating homogeneous shear flow. Effect of different model constants in Eqs. (22) and (25) on the bifurcation diagram. In curves 1, 2 and 3 $\alpha_3 = \alpha_2/2$ and $\alpha_4 = 1/5$. $\mathscr{R} = 1 - \overline{C}_\omega \Omega/S$.

This class of models has equilibria that are independent of Ω and therefore never bifurcate between the solutions $\varepsilon/Sk \neq 0$ and $\varepsilon/Sk = 0$. This is a manifestation of their inability to discriminate between stabilizing and destabilizing effects of a rotating frame of reference.

2.1.2. A model that bifurcates

In the interest of numerical tractability and with an objective to retain the previous success of the $\overline{v^2}$–f model in computing complex non-equilibrium flows, the following constraints are imposed:

1. The linear constitutive relation (2) should be retained;
2. The new model should reduce to its original form in parallel shear flow in an inertial frame of reference; i.e., $C_\mu^*(\eta_1 = \eta_2) = C_\mu$, where $C_\mu = 0.21$.

Consequently, a truncated version of the EASM (Gatski and Speziale, 1993) cannot simply be adopted. That formulation is only suited to a model based on k as the velocity scale, and does not reduce to the standard model ($C_\mu = 0.09$) in non-rotating parallel shear flow.

The present study adopts the bifurcation diagram as the primary tool for the model development, with the following objectives:

1. The model should bifurcate between only two possible stable solutions $(P/\varepsilon)_\infty = (C_{\varepsilon 2}-1)/(C_{\varepsilon 1}^*-1)$ and $(\varepsilon/Sk)_\infty = 0$.
2. The bifurcation diagram should exhibit a maximum value of $(\varepsilon/Sk)_{\max}$ close to $\Omega/S = 0.5$, as indicated by Rapid Distortion Theory (Sahli et al., 1997) for homogeneous shear flow.
3. Restabilization, $P/\varepsilon < 1$, should occur near to $\Omega/S = 0$ and $\Omega/S = 1$ in homogeneous shear flow.

In addition, the asymptotic behavior at large non-dimensional strain-rates ($\eta_1, \eta_2 \gg 1$) should be considered because the model is intended for complex non-equilibrium flows.

It is convenient to introduce a new strain-parameter

$$\eta_3 \equiv \eta_1 - \eta_2 \tag{19}$$

which becomes identically zero in plane parallel shear in an inertial frame of reference. Also let $\mathscr{R}^2 \equiv \eta_2/\eta_1$. At $|\mathscr{R}| = 1$, $\eta_3 = 0$ and the equilibrium solution of the original model, $(\varepsilon/Sk)_\infty = 0.416$, should be retained.

The eddy-viscosity coefficient is written in the form

$$\frac{C_\mu^*}{C_\mu} = \mathscr{F}_1 \mathscr{F}_2, \tag{20}$$

where $\mathscr{F}_1$ and $\mathscr{F}_2$ are introduced to separately determine the model behavior for $|\mathscr{R}| > 1$ and $|\mathscr{R}| < 1$, respectively. It is possible to separate the problem in this way if $\mathscr{F}_1$ and $\mathscr{F}_2$ take values close to one for $|\mathscr{R}| < 1$ and $|\mathscr{R}| > 1$, respectively, outside their intended regions of influence.

Bifurcation occurs where branches (i) and (ii) in (13) meet. Equating (17) to (18) gives

$$\lim_{\eta_1 \to \infty} \eta_1 C_\mu^* = 2.425. \tag{21}$$

This is implicitly the equation for the rotation rate at which the solution bifurcates. It is an important result because it provides the necessary condition for a model to bifurcate; it is necessary that $C_\mu^* \sim \eta_1^{-1}$ as $\eta_1 \to \infty$. Presently, the constraint $\mathscr{F}_1 \mathscr{F}_2 \sim \eta_1^{-1}$ has to be met. These functions are assumed to take the forms $\mathscr{F}_1 \sim \mathrm{O}(1/\eta)$ and $\mathscr{F}_2 \sim \mathrm{O}(1)$ for $\eta \to \infty$. It should be recalled that the constraint $\mathscr{F}_1 = \mathscr{F}_2 = 1.0$ when $\eta_3 = 0$ must also be satisfied.

Since the assumed form of $\mathscr{F}_1$ is similar to the linear eddy-viscosity coefficient obtained by Pope (1975), Eq. (8) guides the form of $\mathscr{F}_1$. Among many possible forms, the following relation is proposed

$$\mathscr{F}_1 = \frac{1}{1+\alpha_1\sqrt{\eta_2}\sqrt{|\eta_3|-\eta_3}}, \tag{22}$$

where α_1 is a free coefficient. The behavior of Eq. (22) is similar to that of Eq. (8) when $\eta_2 \gg \eta_1$. The dependence on η_2 is considered to be of crucial importance since the primary objective is to sensitize the $\overline{v^2}$–f model to rotational strains. In addition, the proposed form of $\mathscr{F}_1$ becomes $\mathscr{F}_1 = 1$ when $\eta_3 > 0$. To demonstrate the effect of $\mathscr{F}_1$, substitute (20) and (22) into (15). Then solving for ε/Sk gives

$$\left(\frac{\varepsilon}{Sk}\right)_\infty^2 = C_\mu\left(\frac{\overline{v^2}}{k}\right)_\infty\left(\frac{C_{\varepsilon1}^*-1}{C_{\varepsilon2}-1}\right)_\infty - \frac{\alpha_1}{2}\mathscr{R}\sqrt{|1-\mathscr{R}^2|-(1-\mathscr{R}^2)} \tag{23}$$

keeping $\mathscr{F}_2 = 1.0$ for simplicity. Consider plane homogeneous shear flow, for which $S = \frac{1}{2}\partial_y U$, $\omega = S$ and

$$\mathscr{R} = (1 - \overline{C}_\omega \Omega/S). \tag{24}$$

Fig. 1 displays the variation of ε/Sk with $\mathscr{R}$ for different values of α_1, see curves 4, 5 and 6. $\mathscr{F}_1$ forces the model to bifurcate to the trivial solution $(\varepsilon/Sk)_\infty = 0$ at a value of $|\mathscr{R}|$ greater than unity, but it does not affect the original behavior of the model for $|\mathscr{R}| < 1$. It should be recalled that $(\varepsilon/Sk)_\infty = 0.416$ in Fig. 1 corresponds to the original model $\mathscr{F}_1 = \mathscr{F}_2 = 1.0$. The location of the bifurcation points can thus be adjusted by varying the free coefficient α_1; as α_1 increases the bifurcation points moves closer together. However, as will be discussed later, a minor adjustment of $\mathscr{F}_1$ is necessary in order for the model to behave properly when $\eta_1 \gg \eta_2$. This is believed to be important in complex flow computations in order to avoid significantly deteriorating results obtained with the original model.

$\mathscr{F}_2$ was introduced to specify the behavior of the model on the solution branch $(\varepsilon/Sk)_\infty \neq 0$ and to force $(\varepsilon/Sk)_{\max}$ to occur at $\mathscr{R} \approx 0$. $\mathscr{R} = 0$ is equivalent to homogeneous plane strain, which is known to exhibit a more rapid growth of turbulent kinetic energy than homogeneous shear. In addition, the constraint $\mathscr{F}_2 = 1.0$ at $\mathscr{R}^2 = 1.0$ must be imposed. The following expression for $\mathscr{F}_2$ is proposed

$$\mathscr{F}_2 = \frac{1+\alpha_2|\eta_3|+\alpha_3\eta_3}{1+\alpha_4|\eta_3|}. \tag{25}$$

If $\alpha_2 + \alpha_3 \geq \alpha_4$ this yields $(\mathscr{F}_2)_{\max}$, and hence $(\varepsilon/Sk)_{\max}$, at $\mathscr{R} = 0$ ($\eta_3 = \eta_1$). In addition, $\mathscr{F}_2 = 1$ for $\mathscr{R}^2 = 1$. It is necessary that $\alpha_3 \leqslant \alpha_2$ to ensure $C_\mu^* \geqslant 0$. Substituting (20) and (25) into (15), keeping $\mathscr{F}_1 = 1.0$ for simplicity, gives the model behavior shown in Fig. 1 for different values of the free coefficients, see curves 1, 2 and 3. It is thus possible to adjust the free coefficients such that $\mathscr{F}_2 \approx 1$ for $|\mathscr{R}| > 1$ while at the same time the model exhibits $(\varepsilon/Sk)_{\max}$ at $\mathscr{R} = 0$. To demonstrate that the present modeling strategy works, the bifurcation diagram using both (20) and (25) in (15) is also displayed in Fig. 1 for one set of free coefficients. It is evident that the functions $\mathscr{F}_1$ and $\mathscr{F}_2$ can essentially be modeled independently.

The final form of the model can be written

$$C_\mu^* = C_\mu\frac{1+\alpha_2|\eta_3|+\alpha_3\eta_3}{1+\alpha_4|\eta_3|}\left(\sqrt{\frac{1+\alpha_5\eta_1}{1+\alpha_5\eta_2}}+\alpha_1\sqrt{\eta_2}\sqrt{|\eta_3|-\eta_3}\right)^{-1}, \tag{26}$$

where the free coefficients α_i are determined with reference to the bifurcation diagram obtained by substituting (26) into (15). The model coefficients are given by $(\alpha_1,\alpha_2,\alpha_3,\alpha_4,\alpha_5) = (0.055,\frac{1}{2},\frac{1}{4},\frac{1}{5},\frac{1}{40})$. As mentioned above, an additional term is added to the final form of $\mathscr{F}_1$ to ensure a well-behaved model when $\eta_1 >> \eta_2$; it enforces $C_\mu^* \sim 1/\sqrt{\eta_1}$. It should be noted, however, that the additional term affects the bifurcation diagram only marginally because $\alpha_5 \ll 1$.

The bifurcation diagram is shown in Fig. 2. It is compared with the EASM of Gatski and Speziale (1993) as well as with the original model. The present model bifurcates to the trivial solution $(\varepsilon/Sk)_\infty = 0$ very close to the EASM, at $\mathscr{R} = \pm 1.39$. This corresponds to $\Omega/S = (+1.06, -0.17)$. The SSG model gives $\Omega/S = (+1.05, -0.16)$ with $C_{\varepsilon1} = 1.50$ and $C_{\varepsilon1} = 1.9$. The solution for the SSG bifurcation points is given in Appendix A.

However, the fact that the model bifurcates to the equilibrium $(\varepsilon/Sk)_\infty = 0$, does not directly imply restabilization of the flow. The turbulent kinetic energy decays only if $P/\varepsilon < 1$. For $|\mathscr{R}| > 1.39$ the variation of P/ε as a function of $\mathscr{R}$ is obtained from the relation (18). (Of course $P/\varepsilon = 1.78$ for $|\mathscr{R}| \leqslant 1.39$.) The present model predicts $P/\varepsilon < 1$ for $|\mathscr{R}| \geqslant 1.73$ corresponding to $\Omega/S = (+1.21, -0.32)$, as shown in Fig. 2. This is reasonably consistent with linear stability values, $\Omega/S = (1, 0)$, for rotating plane shear flow (Sahli et al., 1997). The linearized SSG model gives stability points of $\Omega/S = (+1.17, -0.28)$; the quasi-linear SSG model gives $\Omega/S = (+1.08, -0.19)$. These values are found by setting $P/\varepsilon = 1$ in the formulae in Appendix A.

Restabilization of the flow does not only occur in a rotating frame of reference. Curvature and stratification are other effects for which scalar models should possess the ability of SMCs to bifurcate. In these cases we have observed that the bifurcation point and the point where restabilization occurs are significantly separated. The relevant criterion for calibrating turbulence models in these cases should therefore be where $P/\varepsilon = 1$ rather than where $\varepsilon/Sk = 0$.

As an example of this difference in model behavior, consider homogeneous shear with streamline curvature for which $\eta_1 = 2(Sk/\varepsilon)^2(1-\xi)^2$ and $\eta_2 = 2(Sk/\varepsilon)^2(1+\xi)^2$ (Holloway and Tavoularis, 1992). Here, $\xi \equiv U_c/R_c/2S$ and U_c and R_c denote the axial velocity at the centerline and radius of curvature, respectively, and $S = \frac{1}{2}\partial_y U$. The physical mechanism of curved homogeneous flow is different from the rotating flow in that the equilibrium value of ε/Sk is non-zero for all $\xi \leqslant 0$. The trivial solution $(\varepsilon/Sk)_\infty = 0$ exists only for $\xi > 0$: there is only one bifurcation point. It should be recalled that $\xi = 1$ corresponds to solid body rotation. The present model predicts $(\varepsilon/Sk)_\infty = 0$ for $\xi \geqslant 0.28$ whereas $P/\varepsilon < 1$ for $\xi > 0.59$. Hence, the curvature parameter must be more than doubled after the

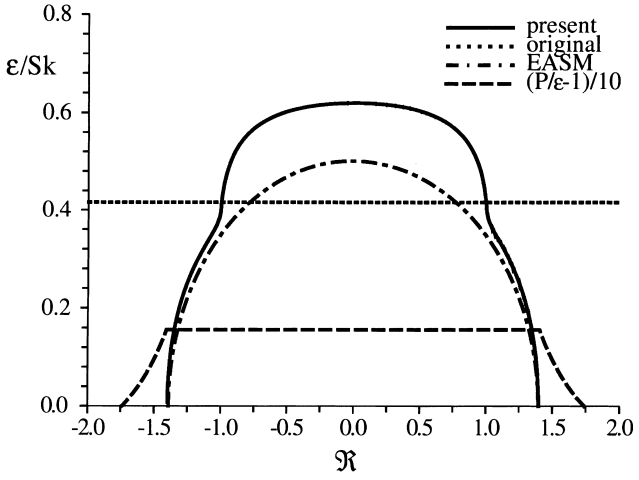

Fig. 2. Rotating homogeneous shear flow. Bifurcation diagrams for the present and original $\overline{v^2}$–f model, and the EASM (Gatski and Speziale, 1993). $\mathscr{R} = 1 - \overline{C}_\omega\Omega/S$.

bifurcation has occurred before the model predicts restabilization of the flow.

Up to this point, the model has been calibrated in rotating homogeneous shear flow. The results suggest that (26) constitutes a viable candidate for further testing in more complicated, non-equilibrium flows for which the model is intended to be used. The set of free model coefficients in (26) have been determined in order to reproduce the behavior of SMCs in rotating homogeneous shear flows. However, in the course of the present study it was found necessary to introduce a dependence on the anisotropy parameter $\overline{v^2}/k$ in (26) for wall-bounded, non-equilibrium flows where the non-dimensional strain-parameters $\eta_1, \eta_2 \gg 1$. The objective is to suppress rapid variations of C_μ^* that can occur in the near-wall viscous region. They have the potential to deteriorate numerical stability. This fault is inherited from the EASM. The final form of the model coefficients are given by

$$\begin{aligned} &C_\mu = 0.21, \quad \overline{C}_\omega = 2.25, \\ &\alpha_1 = 0.055\sqrt{f_1}, \quad \alpha_2 = \frac{1}{2}f_1, \quad \alpha_3 = \frac{1}{4}f_1, \\ &\alpha_4 = \frac{1}{5}\sqrt{f_1}, \quad \alpha_5 = \frac{1}{40}, \end{aligned} \tag{27}$$

where $f_1 = \sqrt{(\overline{v^2}/k)/(\overline{v^2}/k)_\infty}$. The parameter f_1 becomes $f_1 = 1$ in homogeneous shear, so the constants determined above retain their original values. Recall that $(\overline{v^2}/k)_\infty = 0.367$.

The proposed modification (26) and (27) can in principle be used in conjunction with other models, like k–ε. In that case wall damping functions, f_μ, would replace f_1 in low Re versions.

3. Results and discussion

In order to assess the performance of the new model in inhomogeneous turbulent flows, three test cases are considered in this section. These cases were selected with the objective to test the model in flows in which the turbulence field dominates the overall effect of imposed body forces. The success of the predictions therefore relies heavily on the turbulence closure. Model predictions are compared with available experimental and DNS data as well as with results obtained with other turbulence closures, in particular the original $\overline{v^2}$–f model. In summary, the new model is given by Eqs. (2)–(6), (26) and (27) with the solid wall boundary conditions (7).

3.1. Rotating channel flow

The Coriolis body force that arises from an imposed rotation of the reference frame is known to profoundly affect turbulent flow. Depending on the magnitude and orientation of the rotation vector, turbulence can be enhanced or suppressed. The mean flow can be directly altered, or can respond indirectly via the Reynolds stress.

The most frequently used test case for assessing turbulence closures in a rotating frame is fully developed channel flow in orthogonal mode rotation. This configuration has been the subject of a number of experimental and numerical studies (Johnston et al., 1972, 1993). Depending on the sense of rotation, the pressure-driven flow in a channel is subjected to stabilization or destabilization of the turbulence; if the rotation vector Ω is parallel (antiparallel) to the background mean flow vorticity, the turbulence is stabilized (destabilized). The imposed rotation breaks the symmetry of the flow field and may eventually lead to relaminarization on the stable side of the channel. A salient feature of this particular flow is that the rotational effects on the mean flow field enter *only* via the turbulence equations.

Consider fully developed channel flow where $\vec{U} = (U(y), 0, 0)$ subjected to a constant angular velocity $\vec{\Omega} = (0, 0, \Omega)$ about the spanwise z-axis. The streamwise (x) mean momentum equation can be written for constant density flow

$$0 = -\frac{\partial P^*}{\partial x} + \frac{\partial}{\partial y}\left((\nu + \nu_t)\frac{\partial U}{\partial y}\right), \tag{28}$$

where the centrifugal force is absorbed into the mean reduced pressure $P^* = P - \frac{1}{2}\Omega^2(x^2 + y^2)$. Since the mean flow field is unidirectional, the continuity constraint $\partial U_k/\partial x_k = 0$ is automatically fulfilled and $-\partial P^*/\partial x$ is a constant. Here, $y = (0, 2h)$ identifies the positions of the lower and upper walls of the channel. Model predictions are compared to the DNS data reported by Kristoffersen and Andersson (1993) at $Re_* \equiv hu_*/\nu = 194$ and at four different rotation numbers: $Ro \equiv 2h\Omega/U_b = 0.0, 0.1, 0.2, 0.5$. The wall friction velocity u_* is prescribed and kept constant in all the numerical computations conducted in this study, which is consistent with the DNS. Typically 100 grid points were used across the channel at $Re_* = 194$ which is sufficient to ensure a grid independent numerical solution (Pettersson and Andersson, 1997).

The mean velocity distributions across the channel displayed in Fig. 3(a) show the characteristic asymmetry caused

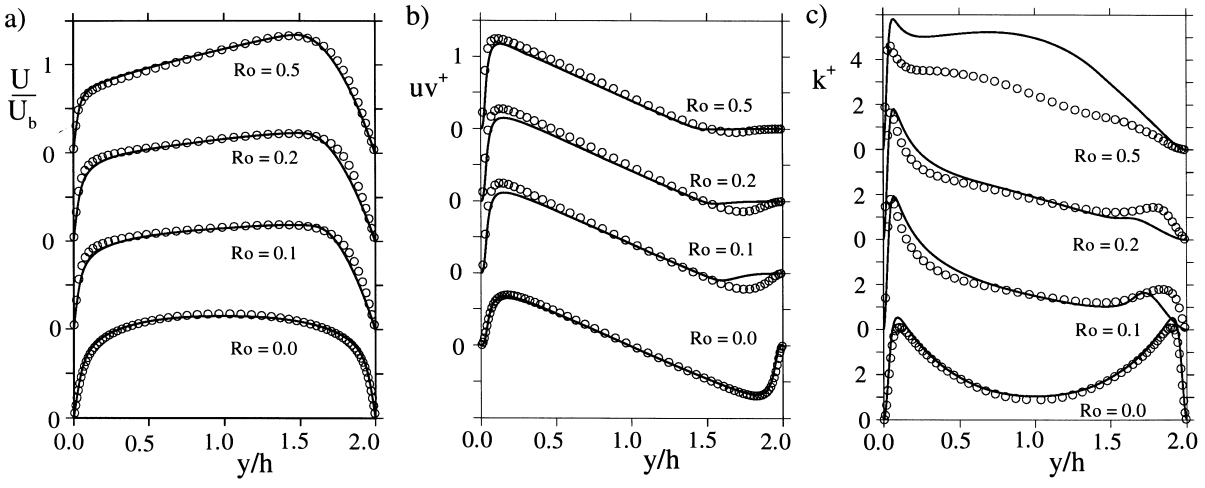

Fig. 3. Rotating plane channel flow. (a) Streamwise mean velocity scaled by U_b, (b) turbulent shear stress and (c) turbulent kinetic energy scaled by u_{*0}^2. Lines: present model, symbols: DNS (Kristoffersen and Andersson, 1993).

by the imposed rotation. The model predictions are in close agreement with the DNS data for all Ro and it is especially encouraging that the model is capable of reproducing the almost irrotational core region in which $dU/dy \sim 2\Omega$. By comparison, the original model returns the same symmetric solution ($Ro = 0.0$) irrespective of Ro. It should also be recalled that the present and original models are identical at $Ro = 0.0$. As Ro increases, the turbulence intensity on the stable side of the channel is reduced, and as shown in Fig. 3(b), the flow eventually relaminarizes. The predicted turbulent shear stress distributions, deduced from (2), are shown in Fig. 3(b). They agree well with the DNS results, although the stabilizing effect of the imposed rotation seems to be overpredicted. The asymmetry of turbulent kinetic energy k across the channel is also well predicted by the model, except at $Ro = 0.5$ where k is significantly overpredicted. This, however, seems not to adversely affect the mean flow and turbulent shear stress distributions.

Due to the rotationally induced asymmetry of the flow field, the friction velocities on the stable (u_{*s}) and unstable (u_{*p}) side of the channel will depend on Ro. Table 1 displays the variation of u_{*p} with Ro. The overall agreement with the DNS data as well as the SMC predictions reported by Pettersson and Andersson (1997) is good and the present model even captures the relative reduction of u_{*p} as Ro is increased from 0.2 to 0.5, in agreement with the DNS results. In order to investigate the Re effect on the wall friction, additional computations was conducted at $Re \equiv 2hU_b/\nu = 2.8 \times 10^4$ for different Ro. The predictions are compared with the DNS data as well as experiments (Johnston et al., 1972) and the SMC predictions (Pettersson and Andersson, 1997) in Fig. 4. The present model faithfully captures the observed Re dependence of the friction velocity, namely that the effect of a given Ro is reduced as Re increases. Recalling that the rotational dependence of the model is based on $\eta_2/\eta_1 \sim \Omega/S$ provides an explanation for the observed Re dependence of the wall-friction velocity: the ratio Ω/S decreases in the near-wall region as Re increases for a given frame rotation Ω, because the mean shear S increases.

3.2. Curved wall boundary layer

Extra strain-rates associated with streamline curvature are probably the most common externally imposed effect on a flow field. In analogy with system rotation, an imposed curvature can either stabilize or destabilize the turbulence. One of the most striking effects is the significant reduction of wall-shear stress observed along a convexly curved surface as compared to a flat plate. This is associated with a stabilization of the turbulence. The reduced turbulence levels imply less mean momentum transport from the free-stream towards the surface whereby, for instance, the tendency for flow separation to occur is increased. The ability to predict the curvature induced suppression of turbulence is relevant in many engineering flows. The baseline experiments of Gillis et al. (1980) and Simon et al. (1982) constitute a well suited test case. These are experimental studies of a developing boundary layer on a

Table 1
Variation of friction velocity along the unstable side of the channel with rotation number at $Re_* = 194$. DNS (Kristoffersen and Andersson, 1993); SMC (Pettersson and Andersson, 1997)

Ro	Present	DNS	SMC
0.10	1.196	1.185	1.204
0.20	1.206	1.217	1.205
0.50	1.201	1.207	1.206

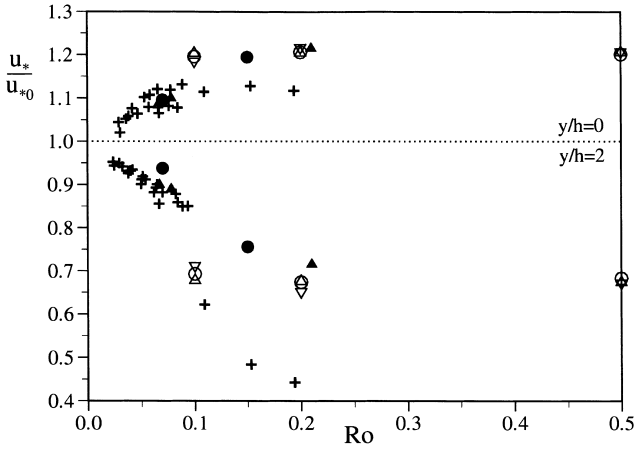

Fig. 4. Rotating plane channel flow. Effect of rotation on local friction velocity u_*/u_{*0} along the stable ($y/h = 2$) and unstable ($y/h = 0$) side of the channel. +: Exp (Johnston et al., 1972); △: SMC (Pettersson and Andersson, 1997); ▽: DNS (Kristoffersen and Andersson, 1993); ○: present. Open symbols $Re \approx 6500$; filled symbols $Re \approx 3 \times 10^4$.

convexly curved surface with zero surface pressure-gradient. The experimental setup consists of a developing flat plate boundary layer that, at a momentum-thickness Reynolds number $Re_m = 4200$, enters a 90° constant-curvature bend with $\delta/R_c = 0.1$, while the zero surface pressure-gradient is maintained. The boundary layer then exits onto another flat plate.

The equations governing the mean flow field are simplified here by invoking the boundary-layer approximation and are given by

$$\begin{aligned}
&\frac{U}{\alpha}\frac{\partial U}{\partial x} + V\frac{\partial U}{\partial y} + \frac{UV}{\alpha R_c} = -\frac{1}{\alpha}\frac{\partial P}{\partial x} + \nu\frac{\partial^2 U}{\partial y^2} - \frac{\partial \overline{uv}}{\partial y} - \frac{2\overline{uv}}{\alpha R_c},\\
&\frac{U^2}{\alpha R_c} = \frac{\partial(P + \frac{2}{3}k)}{\partial y},\\
&\frac{\partial U}{\partial x} + \frac{\partial(\alpha V)}{\partial y} = 0,
\end{aligned} \tag{29}$$

where $\overline{uv} = -C_\mu^* \overline{v^2} T(\partial_y U - U/(\alpha R_c))$ and $\alpha = 1 + y/R_c$. Here (x, y) denotes the directions parallel and normal to the boundary surface, respectively. (U, V) are the mean velocity components in the (x, y)-directions. $y = 0$ on the surface and R_c and δ denote the radius of surface curvature and 99% boundary layer thickness, respectively.

In the present numerical computation, a flat-plate boundary layer was computed downstream to $R_m = 4200$. Curvature was then abruptly introduced by setting $R_c = 10\delta$ and the model was then integrated to a downstream distance $x = 0.7$ m which coincides with the length of the bend reported in the experiments. At $x = 0.7$ m, the recovery was initialized by setting $\delta/R_c = 0$. Although these abrupt changes of surface curvature cause discontinuities, the effect dies away quickly (Durbin, 1993). The free-stream condition was $\partial_y U = -1/\alpha R_c$, $k = 10^{-5}U_\infty^2$, $\overline{v^2} = \frac{2}{3}k$ and $\partial_y \varepsilon = \partial_y f = 0$. To ensure a sufficiently dense computational grid, 104 grid points were used across the boundary layer.

Fig. 5 compares the predicted and measured skin friction distribution, C_f/C_{f0}, normalized on its value at the start of the curvature. The present model responds to the imposed convex curvature ($0 \leqslant x \leqslant 0.7$ m) by suppressing the turbulence intensity which results in a significantly reduced skin-friction. The original model, on the other hand, reveals less sensitivity to the imposed streamline curvature. This shortcoming is expected since the model responds to the surface curvature

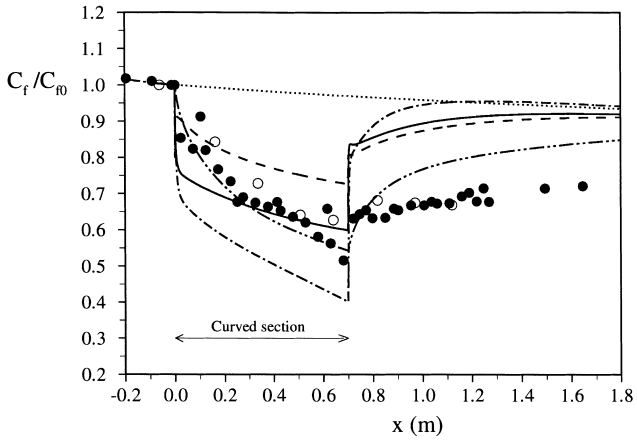

Fig. 5. Convexly curved boundary layer. Skin friction distribution normalized on its value at the start of the curvature ($x = 0$). *Lines*: Computations; ——— : present; – – ––: original; – · · – · · –: SMC (Durbin, 1993); – · – · – : present where Ω was replaced by $-U_c/\alpha R_c$ in (9); · · · · · · · : flat plate. Symbols: Experimental data; open: Gillis et al. (1980); filled: Simon et al. (1982).

solely through the normal pressure-gradient and metric terms that appear when the set of governing transport equations are transformed to cylindrical coordinates. An inherent shortcoming of the eddy-viscosity modeling approach, as compared to the SMC, is the lack of 'memory'-effects; the turbulent shear stress responds instantly to a change in curvature. This is readily seen in Fig. 5, in which the SMC prediction reported by Durbin (1993) is also shown. Both eddy-viscosity models significantly overpredict the initial response to the curvature ($0 \leqslant x < 0.01$ m) as well as the rate of flow recovery on the flat-plate surface following the curved section ($x > 0.7$ m).

Fig. 6 compares experimental data to the predicted mean velocity, turbulent kinetic energy and shear stress distributions across the boundary layer at two different downstream locations: $x = -0.062$ and $x = 0.162$ m. Here, $k^* = k/U_{pw}^2$ and $\overline{uv}^* = \overline{uv}/U_{pw}^2$, where $U_{pw} = \lim_{y\to\infty}(\alpha U)$. It should be noted that the models are identical upstream of the bend ($x = -0.062$ m). Fig. 6(a) shows that the mean velocity profile in the bend is altered from its upstream shape across almost the entire boundary layer. The experimental data, on the other hand, only display an effect of curvature very close to the wall ($y/\delta < 0.15$). This deficiency is also present in SMC predictions (Durbin, 1993). The modification of the $\overline{v^2}$–f model is only effective in the near wall layer where it exhibits a consistent behavior with the experimental results.

The reduction of skin friction in Fig. 5 is associated with a reduction of the turbulent shear stress. Fig. 6(b) displays reduced levels of the predicted uv^* in the bend ($x = 0.162$ m). The present model predicts a lower shear stress than the original model but it is still significantly above the data. The original model predicts the structural parameter $\overline{uv}/k$ to be 0.3 in the logarithmic layer both upstream the bend ($x = -0.062$) and in the bend ($x = 0.162$), whereas the present model predicts an approximately 17% reduction in the bend. The experimental result, on the other hand, indicates a reduction on the order of 25%. Both the present and original model predict almost the same reduction of k^* as the flow enters the bend, as shown Fig. 6(c).

Finally, recall that rotation enters the present model solely through an effective mean intrinsic vorticity W_{ij}^* (Eq. 10). This was derived from the Reynolds stress transport equations in a *non-inertial* frame of reference by Gatski and Speziale (1993). Since the curved wall computation was performed in an inertial frame, the second term in (10) is zero. However, if the same equilibrium analysis were repeated in a cylindrical coordinate system, then metric terms would arise and would cause the angular velocity Ω in (10) to be replaced by $-U_c/\alpha R_c$. Such metric terms are omitted the the algebraic stress approximation. To assess the importance of curvature terms omitted by the EASM, a computation was done in which Ω was replaced by $-U_c/\alpha R_c$. This is also presented in Figs. 5 and 6 As expected, the response of the model to the imposed surface curvature is increased and the turbulent shear stress in the bend is further reduced. This highlights a potential problem with the equilibrium, algebraic stress models: they are not coordinate system invariant. The metric and rotation terms are derived by assuming that equilibrium is attained in a particular coordinate system.

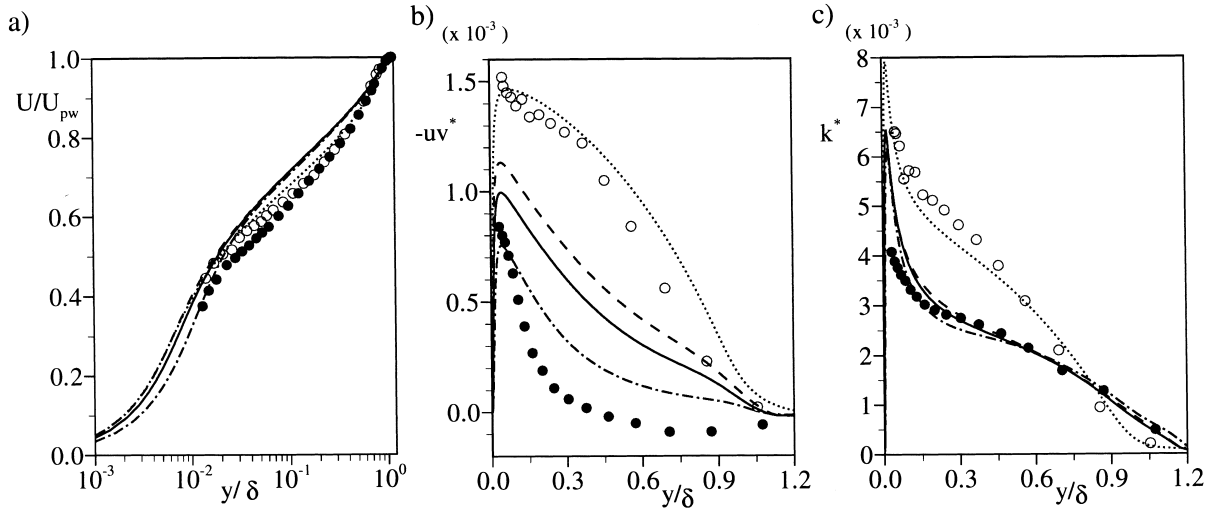

Fig. 6. Convexly curved boundary layer. Predicted distribution of (a) mean velocity, (b) turbulent shear stress and (c) turbulent kinetic energy. *Lines*: computations; Symbols: experiments (Gillis et al., 1980). $x = -0.062$ m: · · · · · · · : present (and original); open symbols. $x = 0.162$ m (20.6° around the bend): — : present; – – ––: original; – · – · – : present where Ω was replaced by $-U_c/\alpha R_c$ in (9); filled symbols.

3.3. Rotating backstep

The flow over a backward facing step is characterized by the simultaneous presence of high shear and streamline curvature in the free shear layer immediately downstream the step. The strained and highly turbulent flow field reattaches further downstream. Rothe (1975) conducted an experimental study of a backstep flow in orthogonal mode rotation. This added the impact of the Coriolis force on the flow field. The experiments revealed a strong correlation between the imposed system rotation and the reattachment length. Nilsen and Andersson (1990) pointed out that the profound effects of rotation could mainly be attributed to changes in the turbulence field. The rotating backstep diffuser studied by Rothe (1975) is therefore adopted in the present study to assess the model performance in a complex geometry.

The backstep diffuser, with the ratio of downstream channel height to the step height (h) of two, was subjected to a constant angular velocity Ω about the z-axis parallel to the step. The x and y axes correspond to the inlet flow direction and wall-normal direction in the inlet channel, respectively. The equations governing the mean momentum and mass continuity are

$$U_k\frac{\partial U_i}{\partial x_k} = -\frac{\partial P^*}{\partial x_i} + \frac{\partial}{\partial x_k}\left(\nu\frac{\partial U_i}{\partial x_k} - \overline{u_i u_k}\right) - 2\epsilon_{ijk}\Omega_j U_k,$$
$$\frac{\partial U_k}{\partial x_k} = 0 \qquad (30)$$

in Cartesian tensor notation. $P^* = P - \frac{1}{2}\Omega^2(x^2+y^2)$ is the mean reduced pressure. The inlet condition (four step heights upstream the step, $x/h = -4$) was prescribed from model computations of fully developed channel flow subjected to spanwise rotation. Fully developed outlet boundary conditions were used at $x/h = 30$. A 190×110 non-uniform grid was used for all calculations. This has proved to be sufficient to ensure grid independence.

Model predictions at two Reynolds numbers $Re \equiv U_b h/\nu = 10^4, 2.8\times10^4$ and different rotation numbers $Ro \equiv \Omega h/U_b$ are compared with the experiments. The only experimental data reported by Rothe (1975) is the variation of reattachment length with Ro. This makes the comparison largely qualitative. Results obtained by Nilsen and Andersson (1990) with a more elaborate implicit algebraic stress model (ASM) are also included. Here, $Ro > 0$ is termed *destabilizing* rotation since the turbulence intensity on the stepped wall upstream the step tends to be enhanced. $Ro < 0$ is referred to as *stabilizing* rotation.

Fig. 7 compares the predicted reattachment length as a function of Ro with experimental and ASM results. The predictions with the present model compare well with the reference data for destabilizing rotation, although the reattachment length in general is somewhat over predicted. The differences between the present predictions and the ASM results seem partly to be an Re effect. It is noteworthy that the model captures the saturation of the rotational effect for sufficiently strong positive rotation as indicated by the ASM results. The effect of stabilizing rotation is, however, too strong. For $Ro < 0$, the experimental results in Fig. 7 show a saturation of the rotational effect on the reattachment length that is qualitatively different from all the model predictions.

It is well known that a reduced turbulence level in the free shear layer will cause the reattachment length to increase significantly. The imposed stabilizing rotation reduces the turbulence level, both along the upstream stepped wall and in the free shear layer. However, Rothe (1975) observed that a series of spanwise vortices persisted far downstream the step in the free shear layer for $Ro < 0$. For $Ro > 0$, on the other hand,

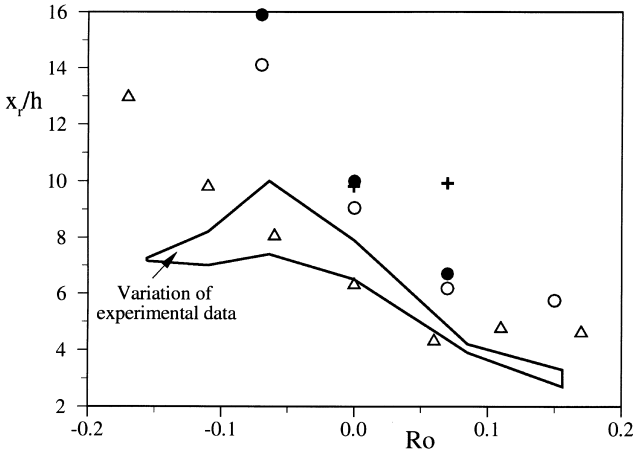

Fig. 7. Rotating backstep. Variation of reattachment length with imposed rotation. △: SMC (Nilsen and Andersson, 1990) at $Re \approx 5500$; +: original $\overline{v^2}$–f at $Re \approx 2.8\times10^4$ and ◯: present $\overline{v^2}$–f; open symbols $Re \approx 10^4$; filled symbols $Re \approx 2.8\times10^4$. Experimental data (Rothe, 1975) $3.0\times10^3 < Re < 2.8\times10^4$.

three-dimensional mixing caused a breakdown of these vortices immediately downstream the step. The three-dimensional mixing is not only related to high turbulence levels caused by destabilizing rotation, but probably also due to large-scale rotational induced secondary flow. The spanwise vortices are believed to provide sufficient mixing in the free shear layer to prevent the reattachment length from becoming very large. This provides a possible explanation for the qualitative difference between the model and experimental results for $Ro < 0$.

Fig. 8 displays computed streamlines for different rotation numbers at $Re \approx 10^4$. The accompanying skin-friction distribution along the bottom wall ($y/h = 0$) is shown in Fig. 9. The intensity of the main recirculation region increases for destabilizing rotation ($Ro > 0$) at the same time as its extent decreases. The length of the main recirculation zone is significantly increased by stabilizing rotation but its intensity is hardly altered. Fig. 8(d) also shows that a recirculation zone on the upper wall ($y/h = 2$) has developed ($2 \leqslant x/h \leqslant 8$) at high destabilizing rotation. It should be noted that the turbulence intensity along the upper wall tends to be reduced for $Ro > 0$.

Finally, it should be noted that the original $\overline{v^2}$–f model predicts approximately the same reattachment length independent of imposed rotation. Since this model only responds to system rotation indirectly through changes to the mean flow field, it can be concluded that the strong correlation between system rotation and reattachment length can be attributed to changes in the turbulence field. This is fully consistent with the findings of Nilsen and Andersson (1990).

4. Concluding remarks

A phenomenological method to sensitize models based on the linear eddy-viscosity hypothesis to rotational effects was developed herein. The general idea is to modify the eddy-viscosity coefficient C_μ by making it a function of velocity-gradient invariants, with the objective to mimic the bifurcations of an EASM. The new C_μ is constrained to reduce to its original value in parallel flow, in an inertial frame of reference. Although the final form of the present model was not based on formal analysis, the principal idea of the method certainly provides a viable alternative to ad hoc Coriolis modifications

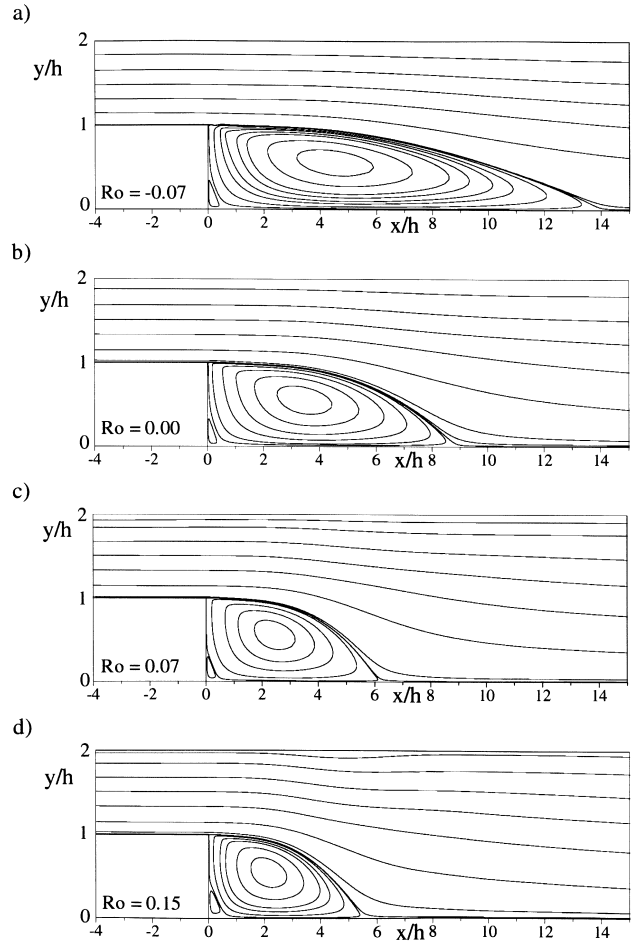

Fig. 8. Rotating backstep. Streamlines predicted by the present model. $Re \approx 10^4$.

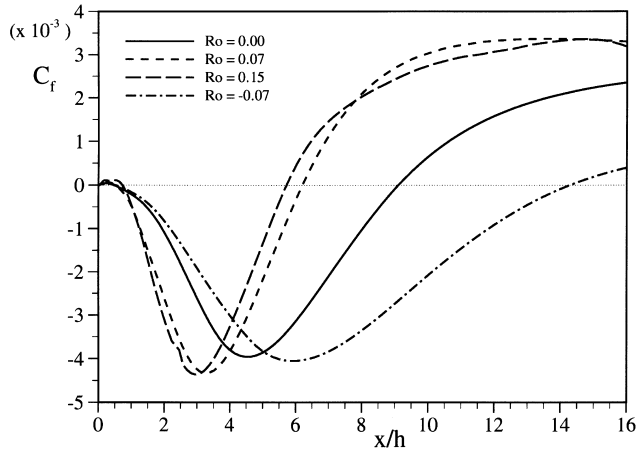

Fig. 9. Rotating backstep. Skin-friction friction coefficient along bottom wall predicted by the present model. $Re \approx 10^4$.

of the dissipation rate equation. The model coefficients were primarily calibrated in rotating homogeneous shear flow.

The methodology was applied to the $\overline{v^2}$–f model. This model was originally developed for non-equilibrium near-wall, but it is a scalar model, insensitive to system rotation.

Three different test cases were used to assess the performance of the model: (i) fully developed channel flow in orthogonal mode rotation, (ii) a developing boundary layer on a convexly curved surface and (iii) a rotating backstep diffuser. A salient feature of these test cases is that the imposed system rotation, or streamline curvature, indirectly affects the mean flow through changes of the turbulence field. The success of the predictions therefore depended strongly on the closure model.

The present model not only captures the augmentation/reduction on the unstable/stable side of a rotating channel, it also reproduces the almost irrotational region in the channel core where $\partial_y U \approx 2\Omega$. The latter effect seems to be closely related to stabilization in rotating homogeneous shear flow: if the model reaches the condition $P/\varepsilon = 1$ at $\Omega/S \approx 1$, it also predicts $\partial_y U \approx 2\Omega$ in the channel core. In exploratory computations it was found that to some extent if restabilization is at $\Omega/S \approx A$ then $\partial_y U \approx 2\Omega/A$ in the core. The core hovers around neutral stability.

Very good agreement was obtained with DNS data. Unfortunately, the only highly accurate reference data available for this test case are very low *Re* DNS data. It is our experience that a model that works well at low *Re* does not necessarily perform equally well at higher *Re*. In order to further improve the predictive capability of the present model in industrial flow computations, higher *Re* reference data is needed.

The prediction of flow strongly affected by convex streamline curvature was also improved relative to the original model. The significant reduction of wall shear stress was captured. However, like any eddy-viscosity model, the dynamic response to the curvature is too prompt. A potential problem with equilibrium algebraic stress models (ASM) for curved flow was also described: the derivation of an ASM assumes that equilibrium is attained in a *particular coordinate system*. An ASM represents an equilibrium solution of a SMC in the chosen coordinate system, but a single ASM can not perform as well as the SMC in a variety of rotating and curved flows.

To assess the model performance in a more complex geometry, a rotating backstep was computed. The strong correlation between reattachment length and imposed system rotation was captured by the model. The original model barely responds to the imposed rotation, which shows that rotational effects enter mainly through the turbulence field. Computational stability was not adversely affected by the new model in any of the cases considered in this study.

Acknowledgements

P.A.D. acknowledges support from the Office of Naval Research, grant #N00014-99-1-0300 and from the Academic Strategic Alliance Program of the US Department of Energy Accelerated Strategic Computing Initiative.

Appendix A

It is possible to solve linear and quasi-linear algebraic stress models in closed form. The bifurcation points for the quasi-linear SSG model are given by Durbin and Shabany (1997) as

$$\mathscr{R} = \pm\sqrt{\frac{x^2}{2a_2^2} - \frac{a_1^2}{3a_2^2}}, \tag{A.1}$$

where

$$x = \frac{c_s^*}{2} + \sqrt{\frac{c_s^{*2}}{4} + \frac{8\ (c_1 + c_1^*\mathscr{P} + \mathscr{P} - 1)}{15\mathscr{P}} + \frac{4}{3}a_1^2}.$$

$\mathscr{R}$ was defined in the text as $\mathscr{R} = \overline{C}_\omega \Omega/S - \omega/S$. The SSG model constants are

$$a_1 = 0.375,\ \ a_2 = 0.8,\ \ c_1 = 1.7,\ \ c_1^* = 0.9,\ \ c_s^* = 0.65,$$

$$\mathscr{P} \equiv P/\varepsilon = (C_{\varepsilon 2} - 1)/(C_{\varepsilon 1} - 1).$$

For the general linear model, $c_s^* = 0 = c_1^*$, this becomes

$$\mathscr{R} = \pm\sqrt{\frac{(c_1 + \mathscr{P} - 1)(\frac{4}{3} - c_s)}{2\mathscr{P} a_2^2} + \frac{a_1^2}{3a_2^2}}, \tag{A.2}$$

where c_s was introduced. The usual value $c_2 = 4/5$ was used in (A.1). Gatski and Speziale (1993) used $c_1 = 3.4$ and $c_s = 0.36$.

Note that bifurcation occurs at particular values of $\mathscr{R}$ in any two-dimensional flow. For example, rotating elliptic flows ($\omega/S > 1$) or hyperbolic flows ($\omega/S < 1$) also bifurcate, according to standard SMC models. Sahli et al. (1997) noted that this property is not consistent with stability theory.

Formulae (A.1) and (A.2) are found by setting $\mathscr{P} = \lim_{\eta_1 \to \infty} \eta_1 C_\mu^*$, by analogy to (21), but the explicit solution to either the linear or quasi-linear SSG model is used for C_μ^*. This determines $\mathscr{P}$ on branch (ii). Setting $\mathscr{P} = (C_{\varepsilon 2} - 1)/(C_{\varepsilon 1} - 1)$ gives the bifurcation points, and setting $\mathscr{P} = 1$ gives the stability points.

References

Durbin, P.A., 1991. Near-wall turbulence closure modeling without "damping functions". Theoret. Comput. Fluid Dyn. 3, 1–13.

Durbin, P.A., 1993. A Reynolds stress model for near-wall turbulence. J. Fluid Mech. 249, 465–498.

Durbin, P.A., Shabany, Y., 1997. Toward consistent formulation of Reynolds stress and scalar flux closures. Fluid Dyn. Res. 20, 115–125.

Gatski, T.B., Speziale, C.G., 1993. On explicit algebraic stress models for complex turbulent flows. J. Fluid Mech. 254, 59–78.

Gillis, J.C., Johnston, J.P., Kays, W.M., Moffat, R.J., 1980. Turbulent boundary layer on a convex curved surface. HMT-31, Department of Mechanical Engineering, Stanford University.

Holloway, A.G.L., Tavoularis, S., 1992. The effects of curvature on sheared turbulence. J. Fluid Mech. 237, 569–603.

Howard, J.H.G., Patankar, S.V., Bordynuik, R.M., 1980. Flow prediction in rotating ducts using Coriolis-modified turbulence models. ASME J. Fluids Engrg. 102, 456–461.

Jongen, T., Machiels, L., Gatski, T.B., 1998. Predicting non-inertial effects wth linear and non-linear eddy-viscosity, and algebraic stress models. Flow Turbulence and Combustion 60, 215–234.

Johnston, J.P., Halleen, R.M., Lezius, D.K., 1972. Effects of spanwise rotation on the structure of two-dimensional fully developed turbulent channel flow. J. Fluid Mech. 56, 533–557.

Kristoffersen, R., Andersson, H.I., 1993. Direct simulations of low-Reynolds-number turbulent flow in a rotating channel. J. Fluid Mech. 256, 163–197.

Launder, B.E., Tselepidakis, D.P., 1994. Application of a new second-moment closure to turbulent channel flow rotating in orthogonal mode. Internat. J. Heat Fluid Flow 15, 2–10.

Nilsen, P.J., Andersson, H.I., 1990. Rotational effects on sudden-expansion flows. In: Engineering Turbulence Modelling and Experiments, Elsevier Science, Amsterdam, pp. 65–72.

Parneix, S., Durbin, P.A., Behnia, M., 1998. Computation of three-dimensional turbulent boundary layers using the V2F model. Flow, Turbulence and Combustion 60, 19–46.

Pettersson, B.A., Andersson, H.I., 1997. Near-wall Reynolds-stress modelling in non-inertial frames of reference. Fluid Dyn. Res. 19, 251–276.

Pope, S.B., 1975. A more general eddy-viscosity hypothesis. J. Fluid Mech. 72, 331–340.

Rothe, P.H., 1975. The effects of system rotation on separation, reattachment and performance in two-dimensional diffusers. Stanford University Dissertation, Department of Mechanical Engineering.

Sahli, A., Cambon, C., Speziale, C.G., 1997. Linear stability analysis of plane quadratic flows in a rotating frame with applications to modeling. Phys. Fluids 9, 2300–2309.

Simon, T.W., Moffatt, R.J., Johnston, J.P., Kays, W.M., 1982. Turbulent boundary layer heat transfer experiments: curvature effects including introduction and recovery. NASA CR 3510.

Speziale, C.G., Abid, R., 1995. Near-wall integration of Reynolds stress turbulence closures with no wall damping. AIAA J. 33, 1974–1977.

Speziale, C.G., Mac Giolla Mhuiris, N., 1989. On the prediction of equilibrium states in homogeneous turbulence. J. Fluid Mech. 209, 591–615.